International Journal of Mass Spectrometry 407 (2016) 69–76

Contents lists available at ScienceDirect

International Journal of Mass Spectrometry

journal homepage: www.elsevier.com/locate/ijms

Characterizing the electronic states of the second-row transition metal cations using high-resolution ion mobility mass spectrometry

Manuel J. Manard[a,*], Paul R. Kemper[b]

[a] National Security Technologies, LLC, Special Technologies Laboratory, 5520 Ekwill St., Santa Barbara, CA 93111, United States
[b] Department of Chemistry and Biochemistry, University of California, Santa Barbara, Santa Barbara, CA 93106, United States

ARTICLE INFO

Article history:
Received 19 May 2016
Received in revised form 11 July 2016
Accepted 15 July 2016
Available online 16 July 2016

Keywords:
High-resolution ion mobility
Collision cross section
Electronic excited states
Transition metal cations

ABSTRACT

Reduced mobilities for ground-state and electronic excited-state configurations of the second-row transition metal cations, excluding Tc^+, have been measured. These values were obtained using an ion mobility mass spectrometer that utilizes a 2 m drift tube to generate high-resolution ion mobility data. Several of these atomic cations have been previously studied and the results obtained here are compared to reduced mobilities reported in the literature. In all cases, ions were generated using pulsed-laser vaporization of either a metal rod or foil target. Presented here for the first time are the reduced mobilities of Y^+, Ru^+, and Rh^+. A discussion of the observed trends in the mobilities of the second-row transition metal series, relative to those measured for the first-row series, is also provided.

1. Introduction

Elucidating the chemical and physical properties of transition metal cations has been the source of considerable study over the last three decades [1–3]. From single atomic cations [4–7] to clusters made up of many atoms [8–10], these ions are of particular interest because of the role they play in complex chemical reactions, such as serving as catalysts for the oxidation of CO [11–13] and saturated hydrocarbons [14,15]. The chemistry associated with these species can be especially complicated due to the large number of energetically low-lying electronic excited states that are readily accessible during the ionization/vaporization processes [16,17]. These excited states are particularly long lived, with radiative lifetimes on the order of milliseconds to seconds. The reason for these relatively long lifetimes is that parity forbidden transitions must occur in order to deactivate the electronic excited states (s to d orbital transitions).

Ion mobility (IM) is an analytical technique that was first developed in the 1950s [18,19]. At its core, IM measures the velocity of an ion traveling through a buffer gas under the influence of an applied electric field. The factor relating the velocity (v) and the electric field (E) is the mobility (K).

$$v = KE \tag{1}$$

Mobilities are usually reported as reduced mobilities (K_0), the mobility at 273 K and 760 Torr.

$$K = K_0 \frac{T}{273} \frac{760}{p} \tag{2}$$

This reduced mobility is determined by the collision cross section of the ion [20]. Mobility measurements have experienced a sizeable resurgence over the past 25 years [21–24] and have been applied to a wide variety of systems ranging from single atoms [25–29] to proteins [30–33]. In recent years, there has been a thrust toward the development of high-resolution IM instrumentation capable of resolving a 1% difference in cross section/mobility. Much of this effort has been focused on resolving multiple stable conformations of relatively large biomolecules in the gas phase [34–36]. Many of these instruments utilize drift tubes ranging in length from approximately 1–2 m to produce high-resolution IM spectra [37–39]. Data now exist demonstrating the capability of applying high-resolution IM to large molecules. However, few examples of high-resolution IM being applied to smaller systems, including atomic ions, are found in the literature. Studies of this type have the potential to elucidate some of the fundamental physical properties of these relatively simple systems, such as resolving metastable electronic excited-states from ground-state configurations.

Previous investigations have applied IM to transition metal cations [25–29]. Kemper and Bowers found that the ground-state electronic configurations of first-row transition metal cations could be distinguished from excited-state configurations using IM [25]. For these ions, the low energy electronic states either have a $3d^n$

* Corresponding author.
E-mail address: manardmj@nv.doe.gov (M.J. Manard).

http://dx.doi.org/10.1016/j.ijms.2016.07.006
1387-3806/

or a $4s3d^{n-1}$ electronic configuration; thus, deactivation from the excited states to the ground state is parity forbidden, allowing them to be characterized. Subsequent studies have applied IM to some of the second- and third-row transition metal cations, yielding similar results [26–28]. In all cases, ions having electronic configurations with occupied s orbitals were shown to have higher mobilities relative to states with only d orbitals occupied. This phenomenon is attributed to the s orbital having a more repulsive interaction with the filled $1s^2$ orbital of helium. This repulsive interaction neutralizes the attractive forces that rise from the charge-induced dipole potential of the cation-He collision, decreasing the capture radius of ions with occupied s orbitals and yielding increased mobilities.

Here, we report the reduced mobilities of the second-row transition metal cations as measured with a high-resolution ion mobility mass spectrometer (IMMS). With the exception of radioactive Tc, the complete second-row series of transition metals has been characterized. Both ground-state and electronic excited-state configurations of the metal cations were generated, and mobilities were measured for all observed configurations. The reduced mobilities reported here are compared to available experimental values in the literature [26–28] as well as theoretical values obtained from calculation [40,41]. In addition to the transition metal cations that were studied previously, the results for the Y^+, Ru^+, and Rh^+ are presented here for the first time.

2. Experimental method

A detailed treatment of the instrument design has been previously provided [42]; thus, only a brief description is given here. An overview of the instrument is shown in Fig. 1. Ions are generated from pulsed laser vaporization of the stationary metal rod or foil target housed in the ion source. A Nd:YAG laser (Continuum, Model NY82-10), with a maximum power output of approximately 400 mJ/pulse operating at 532 nm with a repetition rate of 10 Hz, is used to irradiate the sample. Since only a small fraction of the available power is used for optimum ion formation, no attempt to correlate relative populations of ground and excited states with laser power was performed. The beam is focused through a lens and enters the vacuum chamber through a 2-inch-diameter laser window.

Ions exiting the laser source are collected and guided through the source chamber using an electrodynamic ion funnel [43,44]. The ion funnel uses an RF-modulated electric field, superimposed on a DC gradient, to guide the beam under conditions where the mean-free-path of the ions is much less than the distance being traversed. The funnel interior orifices form an hourglass shape first described by Tang et al. [45]. The funnel contains an ion-trapping region located near the entrance of the drift tube. Here, ions are accumulated and pulsed into the tube, establishing the start time (t = 0) for the mobility measurements. A 90% transmission nickel mesh screen is applied to an electrode at the entrance of the drift tube. This electrode is located 6 mm from the final entrance funnel electrode and serves to both prevent any RF and/or gate pulses from penetrating the drift region and to precisely define the start of the drift potential and drift length. The drift tube measures 2 m in length and is made up of ten, resistively coated glass tubes.

A second ion funnel is located at the exit of the drift tube. The exit ion funnel serves primarily to compress the ion packets that may have become radially diffuse while drifting through the 2 m tube, dramatically increasing the sensitivity of the instrument. A 90% transmission nickel mesh is mounted to the electrode that directly follows the drift tube to prevent RF penetration from the exit funnel into the drift region. It also defines the end of the drift region. The ion funnels at both the entrance and exit of the drift tube essentially eliminate end effects. These effects occur in two ways. (1) Ions can penetrate into the drift space upon entrance (until their kinetic energy is lost through collision). This reduces the effective drift length and can increase the apparent mobility. In the present instrument, the ions are thermalized in the relative high pressure of the source chamber before entering the drift space and no such penetration occurs. (2) A different end effect occurs upon exiting the drift tube. If a pressure-limiting orifice is present, bulk movement of the buffer gas will occur in the space near the orifice over a dimension comparable to the orifice diameter. The ions are carried along with the buffer gas at a velocity higher than the true drift velocity. The effect, again, reduces the effective drift length. The addition of an exit funnel removes the exit orifice from the drift length, since the drift length is then determined by the entrance and exit screens.

After leaving the exit funnel, ions enter a focusing region that collimates the beam into the quadrupole mass analyzer. A set of steering electrodes, situated near the entrance of the quadrupole, is used to both maximize ion transmission through this section of the instrument and to inject a mobility-selected analyte into the quadrupole for mass analysis, if desired. Following mass analysis by the quadrupole, ions are detected with a conversion dynode and electron multiplier.

To collect the mobility data, a pulse of ions is injected into the pressurized drift tube. The pressure in the tube is typically on the order of 1.5–20 Torr. The buffer gas (helium) is flowed into the drift tube to maintain constant pressure. A weak, homogeneous electric field is applied across the length of the tube, causing the ion packet to drift toward the exit. The ion packet is rapidly thermalized by collision with the buffer gas. Ions exiting the tube are then detected as a function of time to establish an arrival time distribution (ATD). The drift field is then varied and a new arrival time determined. This is repeated, generating a plot of ion arrival time versus the ratio of the pressure to the drift voltage (p/V). The reduced mobility of the ions, K_0, is given by Eq. (3):

$$K_0 = \left(l^2 \frac{273}{760T} \frac{p}{V} \frac{1}{t_a - t_0} \right) \tag{3}$$

where l is the length of the drift tube, T is the temperature in Kelvin, p is the pressure of the buffer gas in Torr, V is the drift voltage, t_a is the arrival time of the ions acquired from the center of the ATD peak, and t_0 is the time the ions spend outside of the drift tube. A plot of t_a versus p/V has a slope inversely proportional to K_0 and an intercept equal to t_0:

$$t_a = \left(\frac{p}{V} \frac{273 l^2}{760T} \frac{1}{K_0} \right) + t_0 \tag{4}$$

The collision cross section (σ) is calculated from K_0 using Eq. (5),

$$\sigma = \frac{3e}{16 N_0} \left(\frac{2\pi}{\mu k_b T} \right)^{1/2} \frac{1}{K_0} \tag{5}$$

where N_0 is the number density of the buffer gas at STP (molecules/cm^3), e is the charge of the ion, μ is the ion-buffer gas reduced mass, k_b is Boltzmann's constant, and T is the temperature.

3. Results and discussion

The reduced mobilities of the second-row transition metal cations measured here are summarized in Table 1. All mobilities were measured at an ambient temperature of approximately 295 K. In some cases, electronic excited-state as well as ground-state configurations of the second-row transition metal cations were observed in the ATDs. For the majority of these systems, multiple mobility measurements were made over a range of pressures; thus, the precision of the reported mobility values were also determined. Accordingly, the standard deviations of the measured mobilities,

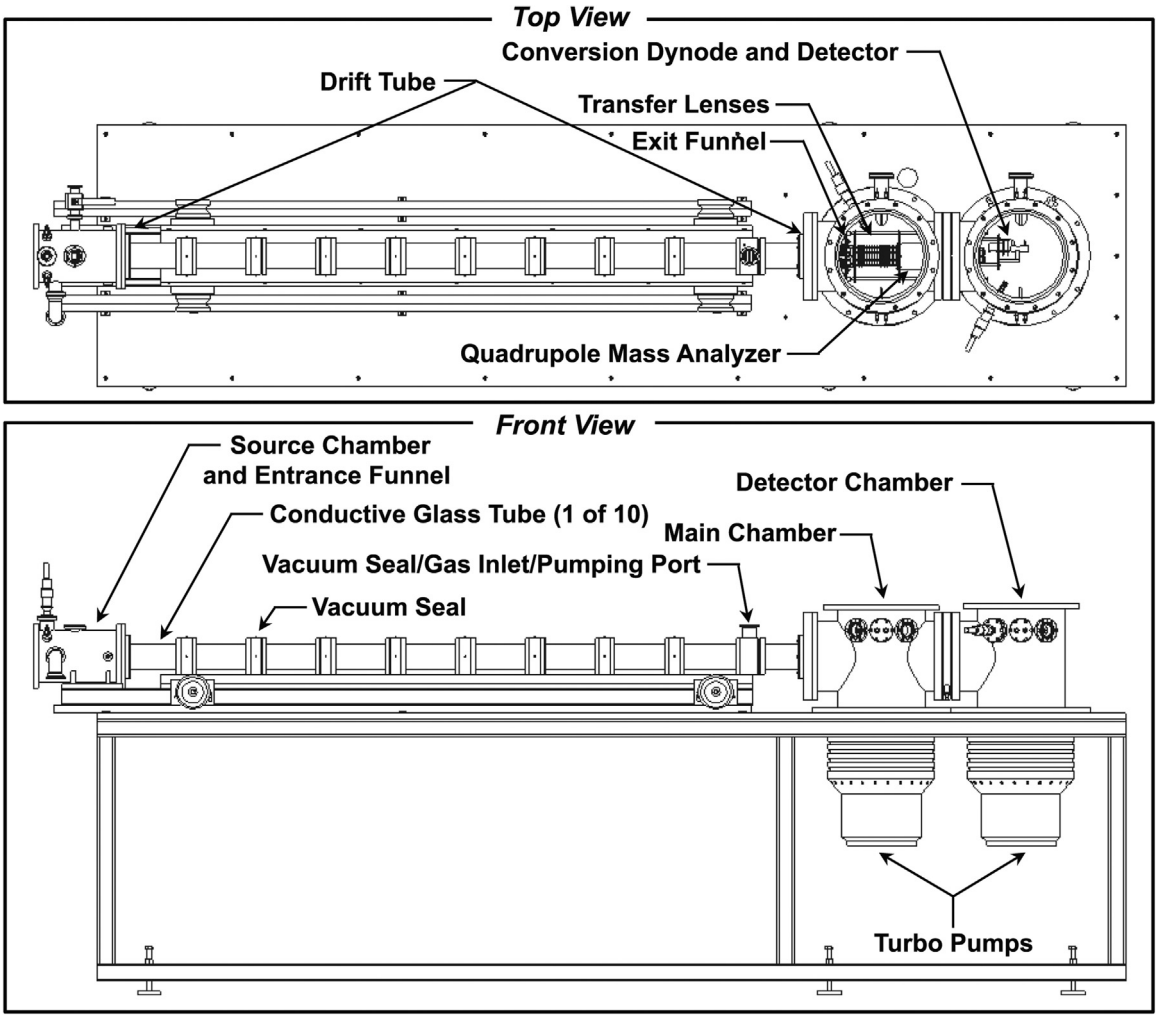

Fig. 1. A schematic representation of the IMMS instrumentation. Essential components that make up the system are labeled. To establish the relative scale of the instrument, the drift tube measures 2 m in length.

Table 1
A summary of the reduced mobilities measured for the second-row transition metal cations.

Ion	Peak	K_0 ($cm^2\,V^{-1}\,s^{-1}$)							
		This Work[a]	Std. Dev.[b]	Number of Exps.[b]	*P* Range (Torr)[b]	Ref. [26][c] (±3%.)	Ref [27]	Ref. [28][c]	Ref. [41]
Y^+	I	**17.1**	0.09	5	1.5–5				
Zr^+	I	**25.0**	0.14	7	1.5–5	25.3			
Nb^+	I	**15.1**	0.04	5	2.5–5	15.5			
Mo^+	I	**19.6**	0.04	4	2.5–10	20.6		18.5 ± 1.9	
Ru^+	I	**17.9**	0.06	5	2.5–10				
Rh^+	I	21.0	0.07	4	5–10				
	II	**17.1**	0.10	4	5–10				
Pd^+	I	21.3	0.04	6	2.5–10	22.9	23.2 ± 0.4		
	II	**17.1**	0.06	6	2.5–10	18.1	18.2 ± 0.6		
Ag^+	I	21.8	0.10	3	2.5–5	22.1			
	II	**17.1**	0.10	5	2.5–10	17.7	18 ± 1		17.4
Cd^+	I	**21.6**	0.03	3	5–10	22.2			21.6

[a] The uncertainty in the mobility values measured as part of this work is ±2%. Ground-state configurations are shown in bold.
[b] Standard deviations reported here are for several separate mobility measurements made for each ion studied over a range of drift pressures (*P*). Thus, the number of experiments that were used to generate the reported values and the drift pressure range are provided.
[c] Only mobilities for peaks corresponding to those observed in the present study are given for clarity in comparison.

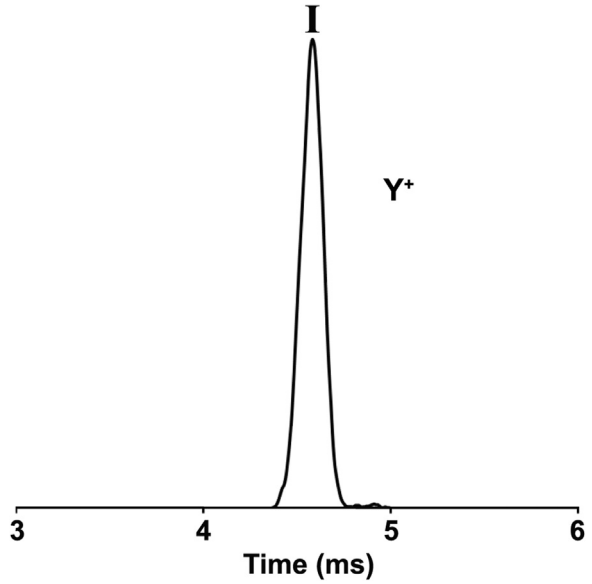

Fig. 2. An ATD of Y^+ acquired at a drift pressure of 2.5 Torr. Ion intensity (y-axis) is in arbitrary units with the zero of intensity at the horizontal axis.

the number of experiments that were used to acquire these values, and the drift pressure range used to generate the mobility measurements are also given in Table 1. A detailed discussion of the expected overall experimental accuracy of the mobilities measured by the instrument (±2%) has been provided elsewhere [42]. When possible, mobilities were acquired using multiple naturally occurring isotopes for a given element to ensure results obtained were free from any potential impurities. Results for the three new systems (Y^+, Ru^+, and Rh^+) are presented first.

3.1. Y^+

The ATD for Y^+ is shown in Fig. 2. One peak is observed in the spectrum. The mobility data is summarized in Table 1. Similar to results obtained for the first-row transition metal series [42], these data demonstrate the high level of precision in the high-resolution mobility measurement.

It has been well established that states containing a single electron in an s orbital have significantly higher mobilities than those containing only d electrons with unoccupied s shells [25,42]. Fewer examples exist of mobilities measured for transition metal cations having a filled s orbital, as is the case here for Y^+. Table 2 provides the assignments and the relative energetics of the low-lying electronic states of Y^+. The ground state of Y^+ is the ^1S state having a $5s^2$ configuration. The single peak in the ATD of Y^+ strongly suggests that it contains the ground-state configuration of the ion. Accordingly, the ATD shown in Fig. 2 is assigned to the ground state $5s^2$ configuration of Y^+.

3.2. Ru^+

The ATD of Ru^+ is shown in Fig. 3. One feature is observed. Similarly to Y^+, the single peak observed in the ATD of Ru^+ suggests that only the electronic ground-state configuration of the ion is present. The mobility data is given in Table 1. Table 2 provides the assignments and the relative energetics of the low-lying electronic states of Ru^+. The $^4F\ 4d^7$ electronic ground-state configuration of the ion is assigned to the peak shown in Fig. 3. The observed mobility is similar to those measured for other late second-row transition metal cations.

Table 2
Low-lying electronic states for the second-row transition metal cations.[a]

Ion	State	Configuration	Energy (eV)
Y^+	^{1}**S**	**5s^2**	**0.00**
	^{3}D	5s4d	0.14
	^{1}D	5s4d	0.41
Zr^+	^{4}**F**	**5s4d^2**	**0.07**
	^{4}F	4d^3	0.39
	^{2}D	5s4d^2	0.54
	^{2}P	5s4d^2	0.73
	^{2}F	5s4d^2	0.76
	^{4}P	5s4d^2	0.96
Nb^+	^{5}**D**	**4d^4**	**0.06**
	^{5}F	5s4d^3	0.39
	^{3}P	4d^4	0.78
	^{3}F	4d^4	0.98
	^{3}H	4d^4	1.22
	^{3}G	4d^4	1.31
	^{5}P	5s4d^3	1.36
Mo^+	^{6}**S**	**4d^5**	**0.00**
	^{6}D	5s4d^4	1.55
	^{4}G	4d^5	1.90
	^{4}P	4d^5	1.96
Ru^+	^{4}**F**	**4d^7**	**0.22**
	^{4}P	4d^7	1.08
	^{6}D	5s4d^6	1.32
	^{2}G	4d^7	1.44
	^{2}P	4d^7	1.72
	^{2}D	4d^7	1.91
	^{2}H	4d^7	1.96
Rh^+	^{3}**F**	**4d^8**	**0.25**
	^{3}P	4d^8	1.21
	^{1}D	4d^8	1.44
	^{1}G	4d^8	1.84
	^{5}F	5s4d^7	2.41
Pd^+	^{2}**D**	**4d^9**	**0.22**
	^{4}F	5s4d^8	3.44
	^{2}F	5s4d^8	4.14
Ag^+	^{1}**S**	**5d^{10}**	**0.00**
	^{3}D	5s4d^9	4.96
Cd^+	^{2}**S**	**5s4d^{10}**	**0.00**
	^{2}P	5p4d^{10}	5.63

[a] Ground states are shown in bold. The energies associated with each state are averaged over J-levels with the zero of energy being the ground state. All values were acquired from Ref. [46].

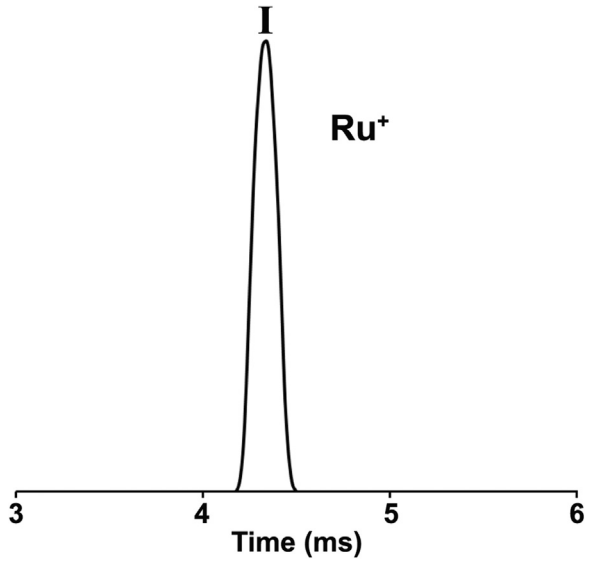

Fig. 3. An ATD of Ru^+ acquired at a drift pressure of 2.5 Torr. Ion intensity (y-axis) is in arbitrary units with the zero of intensity at the horizontal axis.

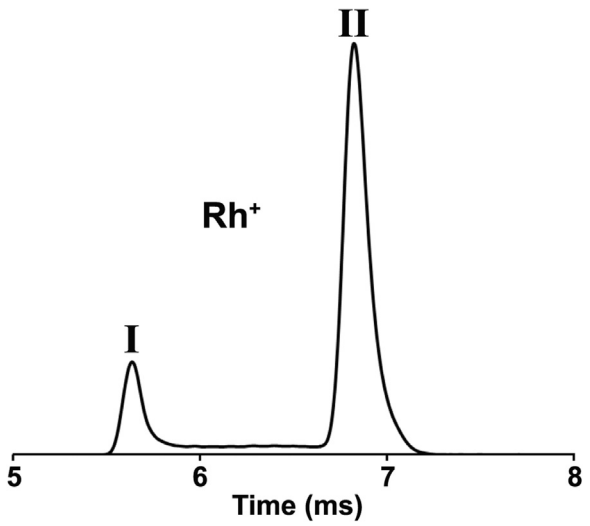

Fig. 4. An ATD of Rh^+ acquired at a drift pressure of 5 Torr. Note the bridging between the two peaks, indicating deactivation of the electronic excited state. Ion intensity (y-axis) is in arbitrary units with the zero of intensity at the horizontal axis.

3.3. Rh^+

Fig. 4 shows the ATD acquired for Rh^+. Two peaks are found in the spectrum, with a significant amount of ion courts observed between the two features. The "filling in" between the peaks is referred to as "bridging". It is caused by collisionally-induced deactivation of the electronic excited state occurring in the drift tube.

The two peaks observed in the ATD of Rh^+ indicate that two electronic configurations of the ion are present. This follows the previously observed first-row transition metal trend where one electronic configuration has a relatively high mobility while the second configuration has a significantly lower mobility. The measured mobilities of the two configurations differ by 18.6% (Table 1), illustrated by the large temporal separation of the two peaks shown in Fig. 4.

Table 2 provides the low-lying electronic states of Rh^+. The ground state of the ion has a $4d^8$ configuration and is likely contained in peak II. Three excited states having this same electronic configuration are observed above the ground state, ranging in energy from 1.21 to 1.84 eV. These states may also be contained in peak II. The first electronic excited state having a $5s4d^7$ configuration is found 2.41 eV above the ground state. Peak I likely contains this excited-state configuration of Rh^+. The bridging between the two features observed in Fig. 4 indicates that a significant amount of collisionally-induced deactivation of the electronic excited-state to the ground-state configuration does occur in the drift tube. A detailed measurement of the deactivation rate of the electronic excited state of Rh^+ will be explored as part of a future effort to measure deactivation rates for second-row transition metal cations where multiple configurations are observed. As will be seen, the later transition metal cations (including Rh^+) are much less prone to deactivation and tend to show multiple peaks in their respective ATDs. This is similar to results obtained for the first-row transition metal cations [42].

3.4. Previously investigated second-row transition metal cations with one mobility peak

ATDs for Zr^+, Nb^+, Mo^+, and Cd^+ are shown in Fig. 5. For each of these second-row transition metal cations, one peak is observed. The mobility data acquired as part of this effort for these cations is summarized in Table 1. In all cases, a high level of precision and repeatability is demonstrated by these results. Table 1 also lists the mobilities previously measured for these transition metal cations. In general, there is good agreement between all measured values. This includes a theoretically calculated mobility for Cd^+ reported by Qing et al. [41,47].

Multiple features were observed in the ATDs of Zr^+, Nb^+, and Mo^+ measured in previous studies. Ibrahim et al. [26] observed two peaks in the ATD of Zr^+. They also observed two peaks in the ATD of Nb^+. Iceman et al. [28] observed two peaks in the ATD of Mo^+, while only peak was observed for ATD of Mo^+ in the study performed by Ibrahim et al.

In the previous studies of Zr^+, the high mobility peak was assigned to the ^4F $5s4d^2$ ground-state configuration. Some low-lying excited states, also having $5s4d^2$ configurations, could also be contained in this peak. The lower mobility peak was said to contain the $4d^3$ electronic excited state of the ion. In the previous Nb^+ study, the ground state, which has a $4d^4$ electronic configuration, was assigned to the peak with the lower mobility. The higher mobility peaks were assigned to the electronic excited state having a $5s4d^3$ configuration. Some controversy is found in the literature for the assignment of the Mo^+ electronic states. Iceman et al. assigned the $4d^5$ ground-state configuration to the lower mobility peak observed in their data and the $5s4d^4$ electronic excited-state configuration to a higher mobility peak. The findings of Ibrahim et al. were less conclusive. The single peak they observed had a mobility of 20.6 $cm^2\ V^{-1}\ s^{-1}$; no definitive assignment was made. No deactivation from the electronic excited states of either Zr^+ or Nb^+ was observed in the respective ATDs acquired by Ibrahim et al. Similarly, no deactivation rate for the excited state of Mo^+ was reported by Iceman et al.

Based on the agreement with mobilities reported in the literature, the ATDs shown in Fig. 5 likely contain the ground-state electronic configurations of Zr^+, Nb^+, Mo^+, and Cd^+. Thus, Fig. 5a contains the ^4F $5s4d^2$ ground-state configuration of Zr^+. Some electronic excited states may have been present but have likely been completely relaxed to the ground state. This hypothesis is supported by the slight asymmetry observed in the ATD of Zr^+, which tails to lower mobilities. Fig. 5b is assigned to the $4d^4$ electronic configuration of Nb^+. The ground state $4d^5$ electronic configuration of Mo^+ is assigned to the ATD shown in Fig. 5c, suggesting that the peak observed by Ibrahim et al. was the ground-state configuration of the ion. The electronic state assigned to the peak in Fig. 5d is the ground state $5s4d^{10}$ configuration of Cd^+. The lack of multiple electronic configurations observed in the ATD of Zr^+, Nb^+, and Mo^+ can be attributed to relaxation of the electronic excited states to the ground state. Although no rates of deactivation have been reported in previous studies, the single peaks observed in the ATDs in Fig. 5 are not unexpected. The increase in collisions that occurs on these significantly longer timescales, relative to all previous experiments, has likely led to deactivation of the electronic excited-state configurations. This was also found when characterizing the first-row transition metal cation series with the 2 m drift tube [42]. The single peak in the ATD of Cd^+ is expected since the first excited state of Cd^+ is both relatively high in energy (5.63 eV above the ground state) and not metastable (having a $5p4d^{10}$ electronic configuration).

3.5. Previously investigated second-row transition metal cations with two mobility peaks

ATDs of Pd^+ and Ag^+ are shown in Fig. 6. For these second-row transition metal cations, two peaks are observed in the spectra. In both cases, a moderate degree of bridging is observed between the two peaks in the respective ATDs. Pd^+ and Ag^+ mobilities measured as part of this effort, as well as values reported in the literature, are given in Table 1. The overall agreement between the previously measured mobilities and those reported here is good, with most values being within the experimental errors of past studies.

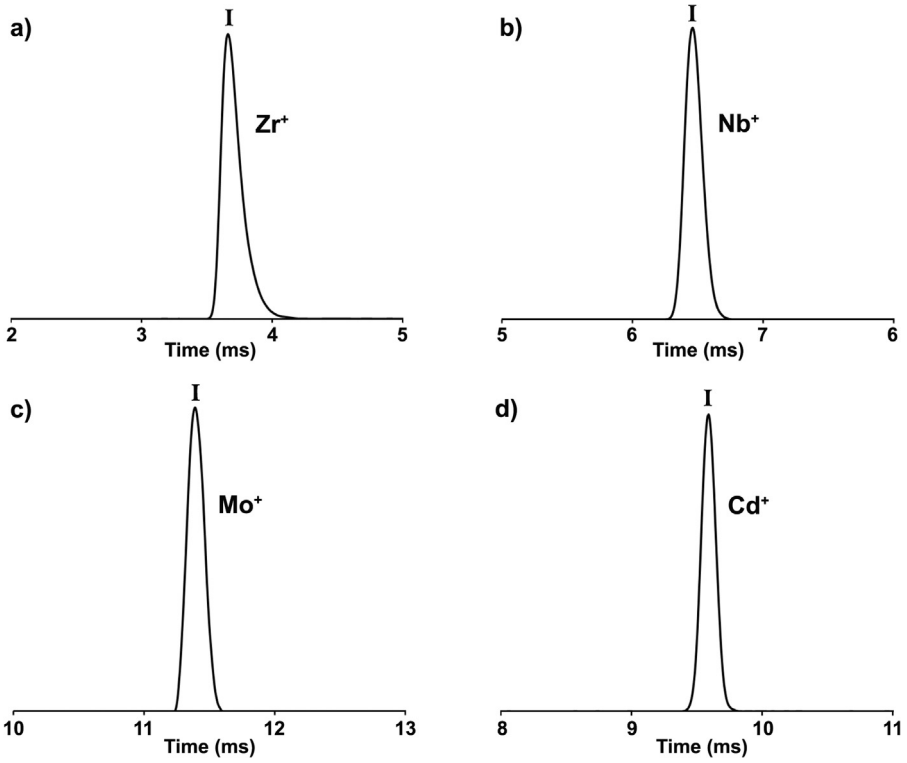

Fig. 5. ATDs of previously investigated second-row transition metal cations where one peak was observed. (a) An ATD of Zr^+ acquired at a drift pressure of 2.5 Torr. Note the slight asymmetry of the peak tailing to longer times. (b) An ATD of Nb^+ acquired at a drift pressure of 2.5 Torr. (c) An ATD of Mo^+ acquired at a drift pressure of 10 Torr. (d) An ATD of Cd^+ acquired at a drift pressure of 10 Torr. In all cases, ion intensities (y-axes) are in arbitrary units with the zero of intensity at the horizontal axis.

Two previous studies have reported on the mobility of Pd^+. Ibrahim et al. [26] and Tayler et al. [27] observed two peaks for Pd^+. In both studies, the peak with the higher mobility peak reported to contain the electronic excited states of the ion having $5s3d^8$ configurations and the lower mobility peak was reported to contain the ground state of Pd^+ having a $4d^9$ configuration. These two previous studies also reported on the mobility of Ag^+. Ibrahim et al. observed two peaks in the ATD of Ag^+, while Taylor et al. only observed one peak. The peak with the higher mobility was reported to contain the ^3D electronic excited state of the ion having a $5s4d^9$ configuration, while the lower mobility peak contained the ^1S ground-state of Ag^+ having a $4d^{10}$ configuration. In addition to the experimental studies, a theoretical investigation calculated the mobility of ground state Ag^+ [41]. Finally, Ibrahim et al. observed a small amount of deactivation for the excited-state configurations of both Pd^+ and Ag^+, and reported an estimated deactivation rate constant for Pd^+ of $6–8\,x\,10^{-14}$ cm^3/s. No deactivation rate for relaxation of the excited state of Ag^+ was given.

Based on the agreement with mobilities reported in the literature, the ground state $4d^9$ configuration of Pd^+ is assigned to peak II (Fig. 6a) and the electronic excited states, having $5s4d^8$ configurations, are assigned to peak I. Similarly, peak I (Fig. 6b) is assigned to the $5s4d^9$ electronic excited states of Ag^+, with peak II containing the $4d^{10}$ ground-state configuration of the ion. For both ATDs shown in Fig. 6, the observed bridging between peaks I and II indicates that deactivation of the $5s4d^{n-1}$ excited states to the $4d^n$ ground states is occurring in the drift tube. The deactivation observed here is more substantial than what was previously measured. This is again attributed to the increase in collisions experienced by the ions in the 2 m drift tube. As previously stated, a detailed measurement of the deactivation rate of the electronic excited states of the second-row transition metal cations will be explored as part of a future effort.

3.6. Observed trends in the reduced mobilities of the first- and second-row transition metal cations

Fig. 7 shows a plot of the reduced mobilities (ground and excited states) of the first- and second-row transition metal cations. The mobilities of the first row have been taken from the literature [25,42], and the mobilities of the second row are values that have been measured as part of this effort. In general, it is clear that the mobilities of the second-row transition metal cations are "intermediate" to those of the first-row cations when corresponding periodic table group members are compared. The term "intermediate" is used to describe the situation observed here where ions with $4d^n$ electronic configurations have higher mobilities than the analogous group member with a $3d^n$ configuration, while ions with $5s4d^{n-1}$ configurations have mobilities that are lower that their $4s3d^{n-1}$ analogs. One exception to this trend is observed for Nb^+, which has a lower mobilities than V^+ with the equivalent electronic configuration. Y^+ also has a lower mobility than either the ground-state or electronic excited-state configurations of Sc^+ ($4s3d$ and $3d^2$, respectively). However, it is important to note that the only observed electronic configuration of Y^+ (ground state, $5s^2$) is unique when compared to those of Sc^+.

Kemper and Bowers described the origin of the large separation in the mobilities of the $4s3d^{n-1}$ and $3d^n$ configurations of the first-row transition metal cations [25]. Briefly, the 4s orbitals of these ions have radii ranging from approximately 1.9–1.4 Å across the first row from Sc^+ to Cu^+ [48]. The hard-sphere radius of helium is 0.6 Å, leading to repulsive interactions at internuclear distances of approximately 2.5–2.0 Å. As previously mentioned, the primary attractive force at play is the charge-induced dipole potential, which has a capture radius of 2.47 Å at 300 K for the first-row transition metal cations [25]. Since this distance is on the order of the M^+-He colliding pair, it leads to a strong repulsive force near the capture radius. This, in turn, promotes grazing collisions where

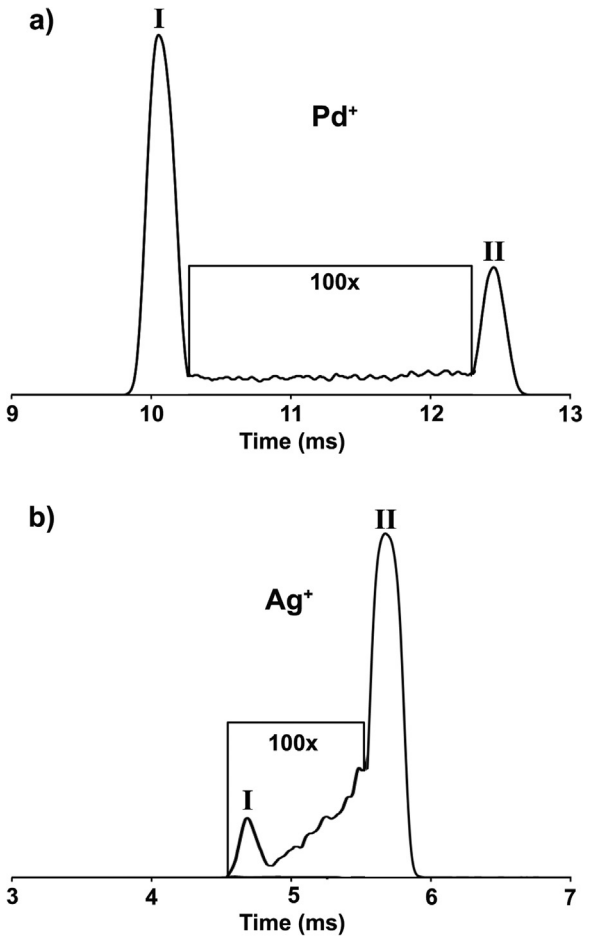

Fig. 6. ATDs of previously investigated second-row transition metal cations where two peaks were observed. (a) An ATD of Pd^+ acquired at a drift pressure of 10 Torr. (b) An ATD of Ag^+ acquired at a drift pressure of 2.5 Torr. In both cases, note the bridging between the two peaks (shown at a magnification of 100×) indicating deactivation of the electronic excited state. Additionally, ion intensities (y-axes) are in arbitrary units with the zero of intensity at the horizontal axis.

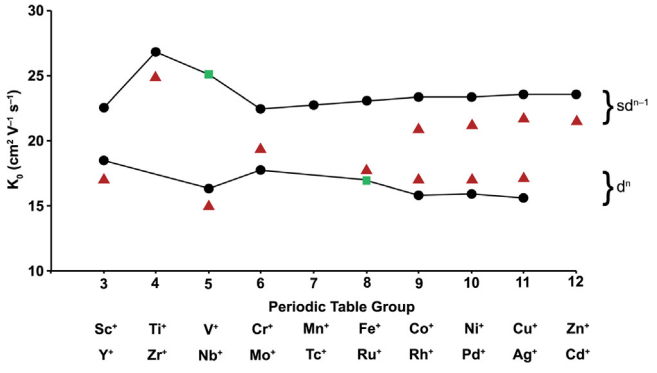

Fig. 7. A plot of the reduced mobilities (ground and excited states) of the first- and second-row transition metal cations. The mobilities of the first-row cations, shown as black dots, were acquired from Ref. [42], while those shown as green squares were acquired from Ref. [25]. Mobilities of the second-row cations were acquired as part of this effort, and are shown as red triangles. The electronic configurations assigned to the mobilities are labeled.

little momentum is transferred. Conversely, the radius of the first-row transition metal cations with $3d^n$ configurations ranges from approximately 0.9–0.5 Å (Sc^+ to Cu^+), yielding M^+-He repulsion at internuclear distances from 1.5 to 1.1 Å. These distances are much less than the capture radius, which allows orbiting (capture) collisions to occur. This leads to significantly reduced mobilities due to the larger momentum transfer in these interactions. A more detailed theoretical discussion is provided by McDaniel and Mason [49].

The interplay between the sizes of valence orbitals with the charge-induced dipole potential of the M^+-He colliding pair can also be used to explain the observed mobility trends of the second-row transition metal cations. For ions with $4d^n$ configurations, the radii of the 4d orbitals are between those of the $3d^n$ and $4s3d^{n-1}$ orbitals of the first-row, ranging from 1.3 to 0.7 Å for Y^+ to Ag^+, respectively [48]. These values lead to M^+-He repulsion at internuclear distances of approximately 1.9–1.3 Å. The capture radius arising from the charge-induced dipole potential is only slightly less than that of the first row (approximately 2.45 Å). This leads to collisions that are less efficient at transferring momentum to the buffer gas for the second-row series of cations ($4d^n$ configurations) when compared to the first row ($3d^n$ configurations). However, this effect is less than that observed for the first-row ions with $4s3d^{n-1}$ configurations and thus, the reduced mobilities of the second-row cations with $4d^n$ configurations are higher than their first-row counterparts with $3d^n$ configurations, while simultaneously being lower than the first-row ions with $4s3d^{n-1}$ configurations.

The situation is different for the second-row transition metal cations having $5s4d^{n-1}$ configurations. Here, the radii of the 5s orbitals are larger than any of the others previously mentioned, ranging in size from approximately 2.0–1.5 Å from Y^+ to Ag^+, respectively. These radii generate a strong repulsive interaction when colliding with He at internuclear distances of approximately 2.6–2.1 Å. As with $4s3d^{n-1}$ configurations of the first row, this repulsive interaction should essentially nullify the charge-induced dipole potential. Thus, the trend of lower mobilities for the $5s4d^{n-1}$ second-row transition metal cations (when compared to their $4s3d^{n-1}$ analogs) is likely not due to the charge-induced dipole potential, but instead may simply result from the increased size of the 5s orbitals compared to the 4s orbitals of the first row [48]. In other words, the ion's larger physical cross section is responsible for the decreased mobility. This relatively straightforward explanation for the observed trend would also account for why the mobilities of the $5s4d^{n-1}$ configurations of Rh^+, Pd^+, and Ag^+ appear to slightly increase when compared to one another, since the orbital radii of these ions slightly decrease across the period. However, it would not explain why the $5s4d^2$ configuration of Zr^+ has a higher mobility than those measured for $5s4d^{n-1}$ configurations of other second-row transition metal ions.

Finally, the two second-row transition metal cations that break the observed trend of having mobilities intermediate those of their first row analogs are both found early in the period. It is clear from the data plotted in Fig. 7 that the early transition metals of both the first and second row behave differently than the systems found later in the period. The mobilities of the early transition metal cations show large oscillations in overall magnitude, whereas the later metal ions tend to exhibit mobility values of similar magnitude. In addition to being early in the second row, Y^+ has a ground-state valence electronic configuration ($5s^2$) that is unique when compared to any other first- or second-row transition metal cation. This observation may account for the mobility of Y^+ breaking from the observed trend. A theoretical study of the mobilities of select lanthanides reported that the fully occupied 6s orbital of Lu^+ ($6s^24f^{14}$ ground-state configuration) has a stronger interaction with helium due to a deeper potential energy well for the attractive interaction than the singly occupied 6s orbital of Yb^+ ($6s4f^{14}$ ground-state configuration) [50]. Experimental mobility data has recently been acquired using the high-resolution IMMS system that supports the results of these calculations. The data indicate that the mobility of Lu^+ is 13.8% lower than the mobility measured for Yb^+. These data will be published as part of a future manuscript on the

mobilities of lanthanide cations. A similar situation could be at play for the fully occupied 5s orbital of Y^+, where a stronger interaction with the buffer gas could account for the relatively low mobility of the cation when compared to the rest of the second-row transition metal cations. For ground state Nb^+ ($4d^4$ configuration), the reason for the relatively low mobility of the ion is not obvious, but suggests that a particularly strong interaction potential could also be involved.

4. Conclusions

Reduced mobilities for ground-state and electronic excited-state configurations of the second-row transition metal cations, excluding radioactive Tc^+, have been measured. For each system, multiple measurements were made and averaged over a range of drift pressures. In all cases, a high degree of precision was found in the acquired mobilities, with typical standard deviations of less than 1% among the measurements. Several of these atomic cations have been previously studied and agreement between the ion mobilities obtained here and values reported in the literature, both experimental and theoretical, are good in most cases. In addition to these ions, the reduced mobilities of Y^+, Ru^+, and Rh^+ are reported here for the first time. Electronic configuration assignments were made for the observed ATDs in accordance with those reported for other second-row transition metal cations, where relatively higher mobility peaks are assigned to contain electronic states having $5s4d^{n-1}$ configurations and relatively low mobility peaks are assigned to contain electronic states having $4d^n$ configurations. A comparison of the mobilities measured for the second-row transition metal series, relative to the first row, has been provided. With the exception of Y^+ and Nb^+, the mobilities of the second-row transition metal cations are "intermediate" to those of the first row (i.e., values measured for the second-row cations with $4d^n$ electronic configurations have higher mobilities than the analogous first-row group member with a $3d^n$ configuration and ions with $5s4d^{n-1}$ configurations have lower mobilities than their $4s3d^{n-1}$ analogs). A discussion of the underlying reasons that may give rise to the observed mobility trend has also been given.

Acknowledgments

The authors would like to acknowledge Howard Bender and the National Security Technologies, LLC, Site-Directed Research and Development (SDRD) program for supporting the completion of this effort. This work was also supported by the U.S. Department of Energy's National Nuclear Security Administration, Office of Defense Nuclear Nonproliferation Research and Development. The work performed here was carried out under the auspices of the Department of Energy, National Nuclear Security Administration, by National Security Technologies, LLC, under Contract No. DE-AC52-06NA25946.

References

[1] M.B. Knickelbein, Annu. Rev. Phys. Chem. 50 (1999) 79.
[2] P.B. Armentrout, in: N.M.M. Nibbering (Ed.), The Encyclopedia of Mass Spectrometry. Volume 4: Fundamentals of, Applications to Organic (and Organometallic) Compounds, Elsevier, Amsterdam, 2005.
[3] K. Eller, H. Schwarz, Chem. Rev. 91 (1991) 1121.
[4] P.B. Armentrout, J.L. Beauchamp, Acc. Chem. Res. 22 (1989) 315.
[5] P.A.M. van Koppen, P.R. Kemper, M.T. Bowers, J. Am. Chem. Soc. 114 (1992) 10941.
[6] M.J. Manard, P.R. Kemper, M.T. Bowers, Int. J. Mass. Spectrom. 241 (2005) 109.
[7] H. Schwarz, Acc. Chem. Res. 22 (1989) 282.
[8] M.J. Manard, P.R. Kemper, M.T. Bowers, Int. J. Mass Spectrom. 249–250 (2006) 252.
[9] P.B. Armentrout, in: P. Jena, A.W. Castleman Jr. (Eds.), Nanoclusters: A Bridge Across Disciplines, Elsevier, Amsterdam, 2010.
[10] M. Moskovits, Metal Clusters, John Wiley & Sons Inc, New York, 1986.
[11] N. Lopez, T.V.W. Janssens, B.S. Clausen, Y. Xu, M. Mavrikakis, J.K. Nørskov, J. Catal. 223 (2004) 232.
[12] M. Haruta, M. Daté, Appl. Catal. 222 (2001) 427.
[13] D.K. Böhme, H. Schwarz, Angew. Chem. Int. Ed. 44 (2005) 2336.
[14] S.K. Buratto, M.T. Metiu, M. Manard, X. Tong, L. Benz, P. Kemper, S. Chrétien-, in: D.P. Woodruff (Ed.), Atomic Clusters: From Gas Phase to Deposited, Elsevier, Amsterdam, 2007.
[15] M. Haruta, Catal. Today 36 (1997) 153.
[16] B.L. Kickel, P.B. Armentrout, J. Am. Chem. Soc. 117 (1995) 764.
[17] B.L. Kickel, P.B. Armentrout, J. Am. Chem. Soc. 117 (1995) 4057.
[18] E.A. Mason, H.W. Schamp Jr., Ann. Phys. 4 (1958) 233.
[19] E.W. McDaniel, Collision Phenomena in Ionized Gases, John Wiley & Sons, Inc, New York, 1964.
[20] E.A. Mason, E.W. McDaniel, Transport Properties of Ions in Gases, John Wiley & Sons Inc, New York, 1988.
[21] G. von Helden, M.-T. Hsu, P.R. Kemper, M.T. Bowers, J. Chem. Phys. 95 (1991) 3835.
[22] D.E. Clemmer, M.F. Jarrold, J. Mass Spectrom. 32 (1997) 577.
[23] T. Wyttenbach, M.T. Bowers, Top Curr. Chem. 225 (2003) 207.
[24] M.T. Bowers, Int. J. Mass Spectrom. 370 (2014) 75.
[25] P.R. Kemper, M.T. Bowers, J. Phys. Chem. 95 (1991) 5134.
[26] Y. Ibrahim, E. Alsharaeh, R. Mabrouki, P. Momoh, E. Xie, M.S. El-Shall, J. Phys. Chem. A 112 (2008) 1112.
[27] W.S. Taylor, E.M. Spicer, D.F. Barnas, J. Phys. Chem. A 103 (1999) 643.
[28] C. Iceman, C. Rue, R.M. Moision, B.K. Chatterjee, P.B. Armentrout, J. Am. Soc. Mass Spectrom. 18 (2007) 1196.
[29] R. Johnsen, F.R. Castell, M.A. Biondi, J. Chem. Phys. 61 (1974) 5404.
[30] S.L. Bernstein, T. Wyttenbach, A. Baumketner, J.-E. Shea, G. Bitan, D.B. Teplow, M.T. Bowers, J. Am. Chem. Soc. 127 (2005) 2075.
[31] K.B. Shelimov, M.F. Jarrold, J. Am. Chem. Soc. 118 (1996) 10313.
[32] R. Roychaudhuri, A. Lomakin, S. Bernstein, X. Zheng, M.M. Condron, G.B. Benedek, M. Bowers, D.B. Teplow, J. Mol. Biol. 426 (2014) 2422.
[33] K.B. Shelimov, D.E. Clemmer, R.R. Hudgins, M.F. Jarrold, J. Am. Chem. Soc. 119 (1997) 2240.
[34] T.D. Do, N.J. Economou, A. Chamas, S.K. Buratto, J.-E. Shea, M.T. Bowers, J. Phys. Chem. B 118 (2014) 11220.
[35] B.C. Bohrer, S.L. Merenbloom, S.L. Koeniger, A.E. Hilderbrand, D.E. Clemmer, Annu. Rev. Anal. Chem. 1 (2008) 293.
[36] L.A. Woods, S.E. Radford, A.E. Ashcroft, Biochim. Biophys. Acta (BBA)—Proteins Proteomics 1834 (2013) 1257.
[37] P.R. Kemper, N.F. Dupuis, M.T. Bowers, Int. J. Mass Spectrom. 287 (2009) 46.
[38] E.S. Baker, B.H. Clowers, F. Li, K. Tang, A.V. Tolmachev, D.C. Prior, M.E. Belov, R.D. Smith, J. Am. Soc. Mass Spectrom. 18 (2007) 1176.
[39] S.L. Koeniger, S.L. Merenbloom, S.J. Valentine, M.F. Jarrold, H.R. Udseth, R.D. Smith, D.E. Clemmer, Anal. Chem. 78 (2006) 4161.
[40] Viehland Database, www.lxcat.net (accessed 17.11.15).
[41] L.A. Viehland, C.C. Kirkpatrick, Int. J. Mass Spectrom. Ion Proc. 149/150 (1995) 555.
[42] M.J. Manard, P.R. Kemper, Int. J. Mass Spectrom. 402 (2016) 1.
[43] S.A. Shaffer, K. Tang, G.A. Anderson, D.C. Prior, H.R. Udseth, R.D. Smith, Rapid Commun. Mass Spectrom. 11 (1997) 1813.
[44] T. Wyttenbach, P.R. Kemper, M.T. Bowers, Int. J. Mass Spectrom. 212 (2001) 13.
[45] K. Tang, A.A. Shvartsburg, H.-N. Lee, D.C. Prior, M.A. Buschbach, F. Li, A.V. Tolmachev, G.A. Anderson, R.D. Smith, Anal. Chem. 77 (2005) 3330.
[46] A. Kramida, Y. Ralchenko, J. Reader, NIST ASD Team 2015 NIST Atomic Spectra Database (ver. 5.3), National Institute of Standards and Technology, Gaithersburg, MD, 2015, accessed 17.11.15 http://physics.nist.gov/asd.
[47] E. Qing, L.A. Viehland, E.P.F. Lee, T.G. Wright, J. Chem. Phys. 124 (2006) 044316.
[48] L.A. Barnes, M. Rosi, C.W. Bauschlicher Jr., J. Chem. Phys. 93 (1990) 609.
[49] E.W. McDaniel, E.A. Mason, The Mobility and Diffusion of Ions in Gases, John Wiley & Sons, Inc, New York, 1973.
[50] A.A. Buchachenko, L.A. Viehland, J. Chem. Phys. 140 (2014) 114309.